Reaction Chemistry & Engineering

ROYAL SOCIETY OF CHEMISTRY

PAPER

View Article Online
View Journal

Cite this: DOI: 10.1039/d5re00313j

Praseodymium-based mixed metal oxides as stable and CO-resistant electrocatalysts for methanol oxidation in acidic media

Pooja and Ravinder Pawar *

In this study, we report for the first time the electrocatalytic performance of Pr-based metal oxides, PrCuO (PCO), PrNiO (PNO), and PrZnO (PZO), toward methanol electro-oxidation. Results show that PCO exhibits superior activity with a low onset potential of 0.96 V *vs.* RHE and strong resistance to CO poisoning. Electrochemical impedance spectroscopy (EIS) reveals a low charge transfer resistance (R_{ct}), indicating fast electron transfer kinetics. Mass activity of PCO reaches 0.75 A mg^{-1}, surpassing the various Pt-based catalysts such as $Pt_{62}Ru_{35}$/C (0.47 A mg^{-1}), $Pt_{62}Ru_{18}Ni_{20}$–O/C (0.30 A mg^{-1}), and PtZn NPs (0.58 A mg^{-1}). Density functional theory (DFT) calculations indicate that PCO facilitates methanol oxidation *via* a COH* intermediate, enhancing CO oxidation and CO_2 evolution. The favorable d-band center and strong Cu 3d–O 2p orbital interaction contribute to its high activity. These findings establish PCO as a promising and durable electrocatalyst for energy conversion applications.

Received 18th July 2025,
Accepted 8th October 2025

DOI: 10.1039/d5re00313j

rsc.li/reaction-engineering

Introduction

Solid oxide fuel cells (SOFCs) have garnered significant interest due to their exceptional energy conversion efficiency and minimal pollutant emissions.[1,2] Operating at elevated temperatures (typically 600–1000 °C), the SOFCs enable direct internal reforming (DIR) of a range of hydrocarbons, including methane, methanol, ethanol, and propane.[3–5] Their remarkable electrocatalytic performance stems from their tunable electronic structures, robust redox properties, and structural flexibility.[5–10] Among various fuel options, methanol stands out as a promising candidate for SOFC applications owing to its high specific energy, liquid state, and ease of storage and transportation.[11–15] Notably, methanol exhibits a higher volumetric energy density (15.8 MJ L^{-1}) than compressed hydrogen (4.5 MJ L^{-1} at 690 bar, 25 °C) and even liquid hydrogen (8.5 MJ L^{-1}), offering logistical advantages.[11,12] Furthermore, as an oxygenated hydrocarbon, methanol is less prone to carbon deposition compared to methane, enhancing its suitability for reforming processes.[11–15] Its complete miscibility with water also allows for easy adjustment of the steam-to-carbon ratio, providing flexibility for various reforming strategies. Nevertheless, the commercialization of methanol-powered SOFC systems remains challenged by the limited performance and durability of available electrocatalysts, for instance, Pt-based materials.[11–15]

Although Pt-based materials are highly active for methanol oxidation, their high cost, limited availability, and susceptibility to CO poisoning, where strongly adsorbed CO intermediates block the active sites and impair catalytic performance, present significant challenges.[16–18] Addressing CO poisoning and enhancing catalyst stability remain critical for the long-term viability of methanol-powered fuel cell technologies.[16–18] In light of these issues, Lanthanide-based metal oxides, composed of elements like La, Pr, Nd, or Sm coupled with late transition metals such as Mn, Fe, Co, Ni, Cu, or Zn, have attracted significant interest due to their ability to balance ionic and electronic transport.[19–29] Among these, transition metals like Ni, Cu, and Zn provide distinct advantages in electrocatalysis: Ni contributes high electrical conductivity and serves as an active site for alcohol oxidation, Cu enhances CO tolerance and stabilizes reaction intermediates, while Zn modulates the electronic structure and promotes oxygen vacancy formation.[27–29] Similarly, praseodymium (Pr)-based oxides have demonstrated significant potential as functional electrocatalytic materials.[30–33] Their inherent properties, including excellent thermal stability, high electrical conductivity, efficient charge transport, and fast ion diffusion, make them suitable candidates for electrode materials.[28–31]

The +3-oxidation state of Pr confirms structural stability, while localized 4f electrons and delocalized conduction bands promote multiple electronic transitions, enhancing catalytic performance.[28–31] Moreover, the presence of

Laboratory of Advanced Computation and Theory for Materials and Chemistry (LACTMC), Department of Chemistry, National Institute of Technology Warangal (NITW), Warangal, Telangana-506004, India. E-mail: ravinder_pawar@nitw.ac.in

intrinsic oxygen vacancies in these oxides facilitates oxygen mobility and contributes to improved redox kinetics.[28–31] Praseodymium-based oxides have recently garnered significant interest in electrocatalysis due to their versatile redox behavior, variable oxidation states (Pr^{3+}/Pr^{4+}), and favorable oxygen mobility.[34] For instance, $PrNiO_3$ and $PrCoO_3$ perovskites have been synthesized *via* accessible gel-based routes and explored for catalytic applications.[35] Notably, structural distortions in $PrNiO_3$ have been shown to dramatically enhance oxygen evolution activity by improving electronic charge transfer.[35] Moreover, Pr_6O_{11} nanorods are effective in promoting CO oxidation, a result attributed to their high lattice oxygen mobility.[34,36,37] In electrocatalytic oxidation of small organic molecules, Pr_2O_3 nanorods supported on Pt/C have demonstrated improved activity for ethanol oxidation, suggesting synergistic interface effects.[37] Finally, broader studies indicate that electronic structure descriptors, such as the oxygen p-band center, offer predictive insight into catalysis across perovskite oxide systems, reinforcing the importance of electronic design in Pr-based catalysts.[38,39] A comprehensive understanding of both the inherent properties and the designed structure of materials is crucial for enhancing their performance across a wide range of applications.[40–50]

While alternative non-precious metal catalysts are under investigation, systematic studies on praseodymium-based transition metal oxides for methanol oxidation remain scarce. The intricate interplay between electronic structure, oxygen mobility, and surface reactivity in these mixed oxides is not yet fully understood. In particular, the *in situ* structural evolution, formation of reactive intermediates, and long-term stability of Ln-based oxides, such as those incorporating Cu, Ni, and Zn with Pr, remain underexplored. Gaining insights into the nature of active species, the dominant reaction pathways, and the synergistic effects among constituent elements is crucial for the rational design of high-performance catalysts.

In this context, we present a comprehensive study on Pr-based metal oxides (PMO), PrNiO (PNO), PrCuO (PCO), and PrZnO (PZO), as anodic materials for the methanol oxidation reaction (MOR). These oxides were synthesized *via* a sol–gel method and characterized using various spectroscopic techniques. The electrocatalytic behavior was evaluated using electrochemical analysis and density functional theory (DFT) calculations were considered to gain mechanistic insights into reaction pathways and active site behavior. Among the investigated materials, PCO exhibited the highest MOR activity, which was attributed to its favorable electronic structure, high active site density, and strong orbital coupling between Cu 3d and O 2p states. The integration of experimental and theoretical approaches in this work provides a fundamental understanding of Pr-based oxides as efficient, CO-tolerant, and durable electrocatalysts, offering a new design strategy for next-generation sustainable materials.

Materials and methods

Chemicals

Praseodymium(III) nitrate hexahydrate ($Pr(NO_3)_3{\cdot}6H_2O$, 99%), copper(II)nitrate trihydrate ($Cu(NO_3)_2{\cdot}3H_2O$, 99%), nickel(II) nitrate hexahydrate ($Ni(NO_3)_2{\cdot}6H_2O$, 99%), zinc nitrate hexahydrate ($Zn(NO_3)_2{\cdot}6H_2O$, 99%), citric acid (CA) ($HOC(COOH)(CH_2COOH)_2$, 99%), and ammonia (NH_3) solution was purchased from Sigma Aldrich. All the chemicals were used as received without further purification. The deionized double distilled (DI) water was obtained from ultrafiltration (Milli-Q, Millipore) units.

Synthesis of PCO, PNO, and PZO catalyst

For the typical sol–gel synthesis, 2.0 g of $Pr(NO_3)_3{\cdot}6H_2O$ and 1.0 g of $Cu(NO_3)_2{\cdot}3H_2O$ were dissolved in 25 mL of DI water to form a homogeneous solution, which was stirred until the metal salts completely dissolved. A molar ratio of 1 : 1 of citric acid (CA) to the sum of Pr and Cu (CA: Pr + Cu) was added to create a complex precursor under magnetic stirring. The pH of the solution was maintained at approximately 2 using 5% ammonia water, and the mixture was stirred for 1 h at room temperature. Subsequently, the resulting sol was dried completely at 90 °C to form a gel precursor. The gel was then heated at 900 °C for 2 h to obtain crystallites of PCO. A similar procedure was followed for the synthesis of PNO and PZO catalyst, where $Ni(NO_3)_2{\cdot}6H_2O$ and $Zn(NO_3)_2{\cdot}6H_2O$ salts were used instead of $Cu(NO_3)_2{\cdot}3H_2O$, respectively.

Electrochemical analysis

The MOR measurements were conducted using a MTX electrochemical workstation equipped with a three-electrode system. An Ag/AgCl electrode served as the reference electrode, while a Pt electrode was employed as the counter electrode. The catalyst ink was prepared by dispersing 2.0 mg of catalyst in a mixture comprising 200 μL of isopropanol and 10 μL of Nafion (5%). Subsequently, the ink was ultrasonicated for 30 min to ensure a homogeneous dispersion of the catalyst. The resulting ink was then deposited onto the surface of a glassy carbon (GC) electrode with a diameter of 5 mm and air-dried.

The electrochemical impedance spectra (EIS) were recorded at the frequency range from 1000 kHz to 10 MHz in 0.5 M H_2SO_4 + 0.5 M CH_3OH solution with 12 points per decade. The chronoamperometry (CA) experiment of MOR was tested for 10 hours in 0.5 M H_2SO_4 solution. In the CO stripping experiments, the electrode was first immersed in 0.5 M H_2SO_4 and subjected to N_2 gas purging for 30 min to remove any dissolved oxygen. Next, CO gas was introduced for 1 h, allowing the CO molecules to adsorb onto the active sites of the electrocatalyst. Finally, N_2 gas was used again to purge the solution, eliminating any dissolved CO. The CO stripping curve was performed in 0.5 M H_2SO_4 solution at a scan rate of 10 mV s^{-1}.

Computational details

To investigate the structure, stability, and electronic properties of the systems under consideration, DFT calculations were carried out using the Vienna *ab initio* simulation package (VASP). The ion cores were represented using projector augmented wave (PAW) potentials.[51] The electron exchange and correlation energies were modeled using the Perdew–Burke–Ernzerhof (PBE)-sol generalized gradient approximation (GGA).[52–55] A plane wave energy cutoff of 520 eV was utilized, with valence electron configurations for Pr: $4f^3\ 6s^2$, Ni: $3d^8\ 4s^2$, Cu: $3d^{10}\ 4s^1$, Zn: $3d^{10}\ 4s^2$, O: $2s^2\ 2p^4$, C: $2s^2\ 2p^2$, and H: $1s^1$. Monkhorst–Pack sampling was employed on the Brillouin zone, using a Γ-centered grid of 4 × 4 × 4.[56] Geometry optimization was conducted until the energy variation reached below 10^{-6} eV, with forces acting on each atom below 0.003 eV $Å^{-1}$.

The change in Gibbs free energy (ΔG) for each reaction step was calculated using Nørskov *et al.* method.[57,58] Under experimental conditions (U = 0, pH, pressure = 1 bar, temperature = 298 K), the free energy ΔG is calculated as follows:

$$\Delta G = \Delta E + \Delta \mathrm{ZPE} - T\Delta S + \Delta G_{\mathrm{U}} + \Delta G_{\mathrm{pH}}, \quad (1)$$

The detailed methodology used in the present investigation is provided in the (SI).

Results and discussion

Synthesis and characterisation of the catalysts

The synthesis protocol for PNO, PCO, and PZO catalysts is schematically illustrated in the SI (Fig. S1). A sol–gel method was employed due to its simplicity, reproducibility, and effectiveness in producing homogeneously porous structures. The morphological and structural properties of the synthesized catalysts were thoroughly characterized using various analytical techniques. Field emission scanning electron microscopy (FESEM) was utilized to investigate the surface morphology. The FESEM images revealed densely packed microstructures for all three catalysts, with uniformly distributed grains approximately 1 μm in size (SI, Fig. S2(a–c)). The FESEM image of praseodymium oxide shows aggregated irregular micro-particles with rough surfaces, which serve as the parent morphology before transition-metal incorporation (SI, Fig. S2(i)). Upon incorporation of transition metal atoms (Cu, Ni and Zn), significant morphological changes are observed. PCO exhibits spherical, capsule-like nanostructures, PNO shows aggregated polyhedral-like particles with rough facets, and PZO displays well-defined hexagonal-like microcrystals, as shown in SI, Fig. S2. Energy-dispersive X-ray spectroscopy (EDS) confirms the presence of all elements in the corresponding catalysts with appropriate stoichiometric ratios, further supporting the successful synthesis of the PMO catalyst (SI, Table S1).

X-ray photoelectron spectroscopy (XPS) was performed to investigate the surface chemical composition and oxidation states of the elements. Spectral deconvolution was carried out using a Gaussian–Lorentzian mixed function (Fig. 1). The O 1s spectra of PCO, PNO, and PZO (Fig. 1a, d, g) exhibited two characteristic peaks: the lower binding energy component (528.09–528.90 eV) corresponds to lattice oxygen (O_{lat}), while the higher binding energy peak (531.08–531.45 eV) is attributed to surface-adsorbed oxygen species (O_{ad}).

In the Cu 2p region of PCO (Fig. 1b), two well-defined peaks were observed at 933.32 eV (Cu $2p_{3/2}$) and 954.15 eV (Cu $2p_{1/2}$), with a spin–orbit splitting of 20.4 eV, confirming the presence of Cu^{2+}. No signals corresponding to Cu^{+} were detected. In addition, a satellite peaks were observed at 950.51 eV. The peak at 928.76 eV corresponds to Pr $3d_{5/2}$. For PNO (Fig. 1e), the Ni 2p spectrum displayed multiple peaks: 854.42 and 873.02 eV corresponding to Ni^{2+}, 856.42 eV to Ni^{3+}, along with satellite peaks at 861.60 and 880.19 eV. In the case of PZO (Fig. 1h), the Zn $2p_{3/2}$ and Zn $2p_{1/2}$ peaks appeared at 1022.25 and 1044.88 eV, respectively, consistent with the Zn^{2+} oxidation state. For all three catalysts (PCO, PNO, and PZO), the Pr 3d spectra exhibited characteristic peaks at ~928.57 and 933.73 eV (Pr $3d_{5/2}$) and 950.42 and 954.38 eV (Pr $3d_{3/2}$), as shown in Fig. 1c, f, and i. Additionally, the Pr 3d XPS spectrum displays two pairs of peaks assigned to Pr^{3+} (~930.0 and 950 eV) and Pr^{4+} (~933.0 and 954.30 eV), further validating the introduction of Pr-based oxides. Detailed XPS fitting results and quantitative analysis are provided in the SI (Table S1 and Fig. S3). The surface composition of the synthesized catalysts, as determined from XPS, corresponds to PCO ($Pr_1Cu_{0.04}O_{2.22}$), PNO ($Pr_1Ni_{0.20}O_{2.52}$) and PZO ($Pr_1Zn_{0.17}O_{2.15}$), confirming the successful incorporation of Cu, Ni, and Zn into the Pr–O matrix.

To gain deeper insights into the structural details of the mixed metal oxides, high-resolution transmission electron microscopy (HRTEM) was performed. Fig. 2a–c shows the HRTEM images of PCO, PNO, and PZO, respectively. These images provide detailed views of the nanostructures, including particle size, morphology, spatial arrangement, and possible interfaces within the composite structures, thereby contributing to a comprehensive understanding of structure–property relationships in these mixed oxides. The HRTEM analysis reveals that the samples exhibit well-defined atomic-scale features, although minor wrinkles were observed at the edges, likely due to sample preparation. High-magnification HRTEM images of PCO, PNO, and PZO show interlayer spacings corresponding to the (004), (103); (113), (111); and (113), (104) planes, respectively. These values were determined from the lattice fringes in the HRTEM images and provide valuable insights into the crystallographic arrangement and phase purity of the materials.

Selected area electron diffraction (SAED) patterns, recorded with an aperture size of ~5 nm (Fig. 2a′–c′), exhibit bright diffraction spots arranged in concentric rings, confirming the polycrystalline nature of the materials. These

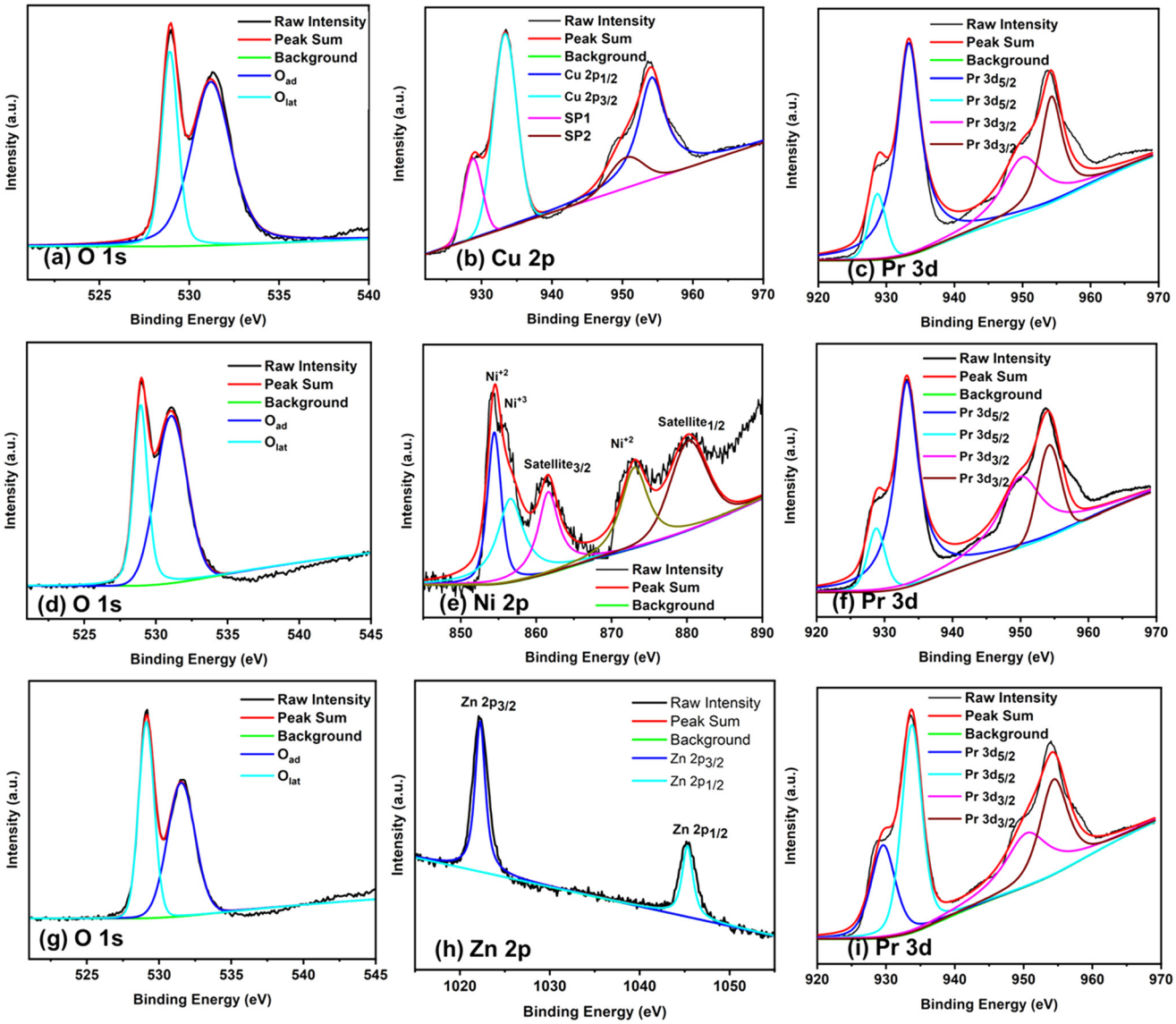

Fig. 1 XPS spectra of (a–c) PCO: O 1s, Cu 2p, and Pr 3d; (d–f) PNO: O 1s, Ni 2p, and Pr 3d; and (g–i) PZO: O 1s, Zn 2p, and Pr 3d.

SAED results are consistent with XRD findings, further verifying the successful formation of the mixed metal oxides. In addition, energy-dispersive X-ray spectroscopy (EDX) and elemental mapping were carried out to analyze the samples, confirming both the elemental composition and the spatial distribution of the elements. High-angle annular dark-field scanning transmission electron microscopy (HAADF-STEM) combined with EDS mapping (SI, Fig. S4) demonstrates the homogeneous distribution of Pr, Cu/Ni/Zn, and O throughout the catalyst matrices, validating the uniform incorporation of all constituent elements.

The interlayer spacings observed in the HRTEM images correlate well with the d_{khl} values obtained from powder X-ray diffraction (PXRD) analysis. The PXRD patterns (SI, Fig. S5) exhibit broad diffraction peaks, characteristic of nanocrystalline materials. The lattice cell constants evaluated from the experimental PXRD data are $a = b = 8.07$ Å for PCO, $a = b = 7.92$ Å for PNO having tetragonal phase with $I4/mmm$ space group. The result is consistent with the various literature support.[59–65] The PZO shows features indicative of a Pr–Zn mixed oxide composite. The small variation in the lattice vector for the synthesized material is attributed to lattice distortion.[59–65] Collectively, these structural and compositional analyses confirm the successful synthesis of single-phase Pr-based mixed metal oxides.

The physical properties of the catalysts were investigated using N_2 adsorption–desorption isotherms and pore size distribution analysis, as shown in the SI (Fig. S6). All three samples exhibited type IV isotherms with clear hysteresis loops, characteristic of mesoporous materials. The pore size distribution of the catalysts reveals pores predominantly in the 2–10 nm range, consistent with the definition of mesoporosity (pore diameters between 2 and 50 nm). The Brunauer–Emmett–Teller (BET) surface areas of PCO, PNO,

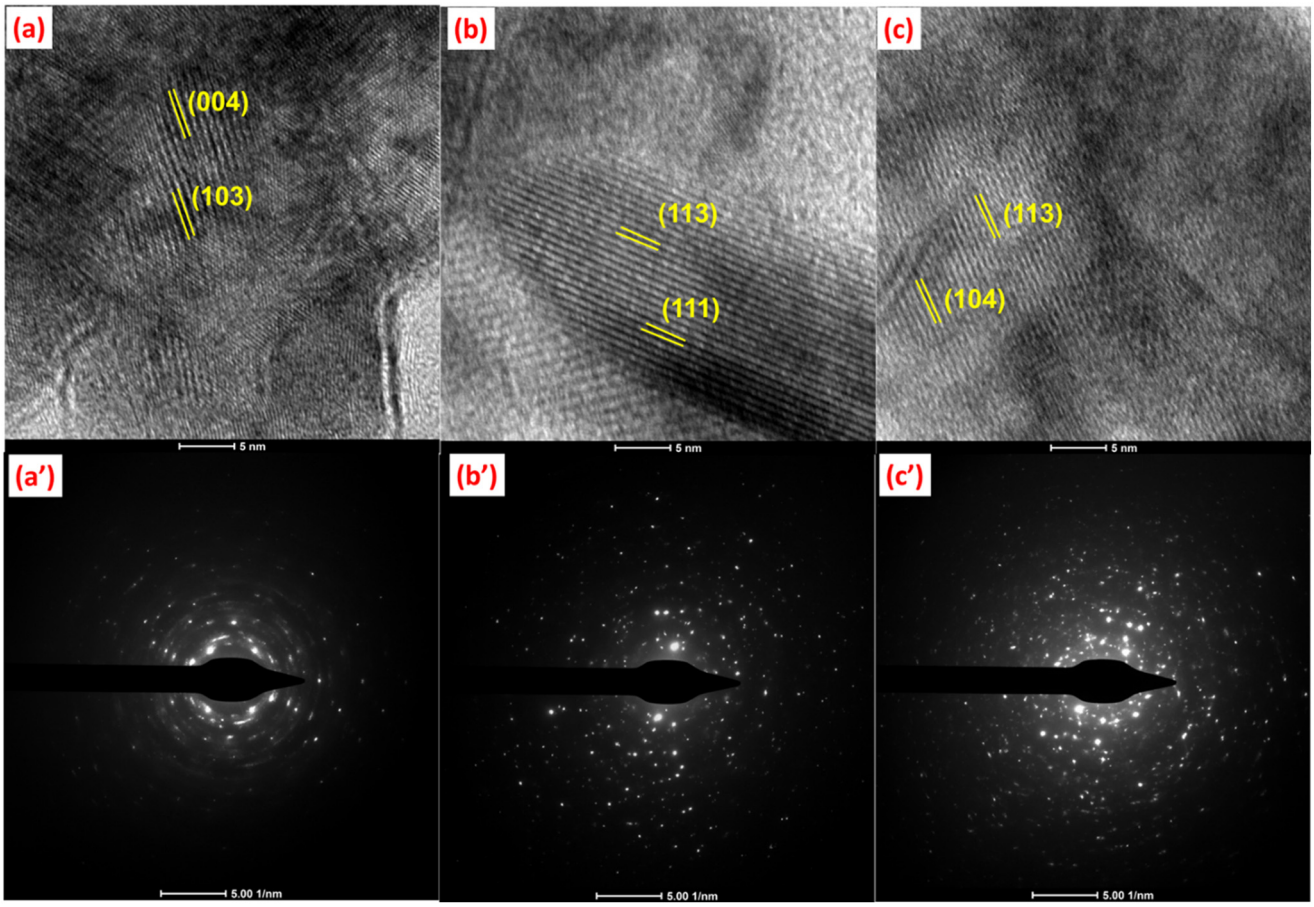

Fig. 2 (a)–(c) represents the HRTEM images of PCO, PNO, and PZO, respectively. (a′)–(c′) represents the SAED images of PCO, PNO, and PZO, respectively.

and PZO were determined to be approximately 4.63, 10.27, and 22.22 $m^2\ g^{-1}$, respectively. Pore size distributions, derived using the Barrett–Joyner–Halenda (BJH) method, revealed total pore volumes of 0.064, 0.10, and 0.20 $cm^3\ g^{-1}$ for PCO, PNO, and PZO, respectively. The mesoporous structure of these catalysts facilitates enhanced mass transport and active site accessibility, thereby contributing to improved electrocatalytic activity. The experimentally obtained structural models of the Pr-based mixed oxides were subsequently employed for the DFT calculations to gain deeper insights into their catalytic behavior.

Density functional theory calculations

Prior to experimental evaluation of MOR performance, systematic DFT calculations were performed to investigate the catalytic behavior of the synthesized praseodymium-based metal oxides. The supercells for PCO, PNO, and PZO were constructed based on experimentally derived crystallographic data. The calculated lattice parameters for the DFT-optimized structures were approximately a = 7.97 and b = 7.97 Å, with minor variations in the third decimal place depending on the transition metal (Cu, Ni, or Zn). The experimental PXRD-derived lattice constants were a = 8.07, b = 8.07 Å for PCO; a = 7.92, b = 7.92 Å for PNO; and a = 7.91, b = 7.91 Å for PZO. The deviation of ~1.2% for PCO, 0.62% for PNO, and 0.75% for PZO are attributed to lattice distortion, with the more pronounced deviation in PCO likely resulting from Jahn–Teller effects.[66]

The optimized geometries of the PMO catalysts and their interaction with methanol are illustrated in Fig. 3. Notably, the adsorption behavior of methanol varies with the nature of the incorporated 3d transition metal. The calculated distances between the methanol molecule and the nearest surface atoms were 2.048 Å (PCO), 3.064 Å (PNO), and 4.360 Å (PZO), respectively. Among these, PCO exhibited the strong adsorption, suggesting a more favorable interaction with methanol compared to PNO and PZO. Key geometrical parameters supporting this observation are also presented in Fig. 3.

Energetics

To gain deeper insight into the nature of methanol–catalyst interactions, periodic energy decomposition analysis (PEDA) was performed using Amsterdam Density Functional (ADF).[67,68] The computational methodology of PEDA is detailed in the SI. All calculations were carried out using

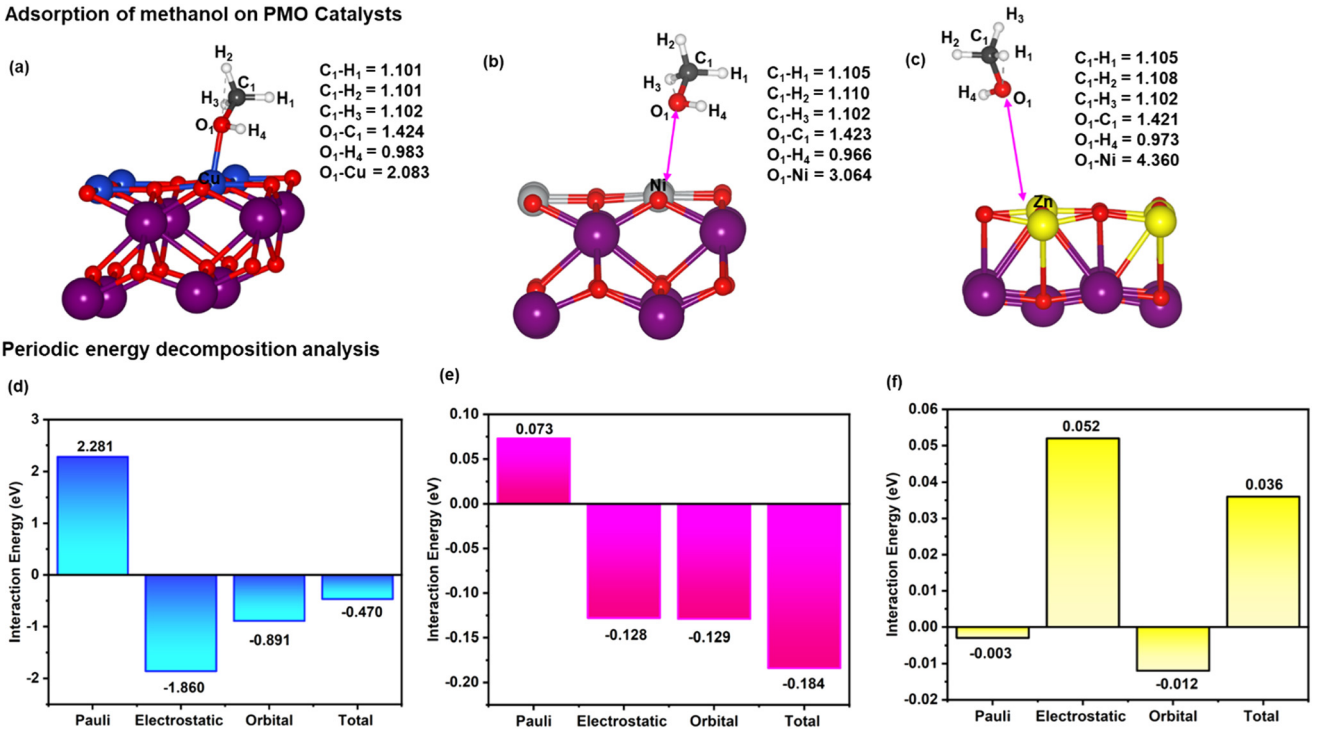

Fig. 3 Schematic representation of the optimized geometrical parameters for methanol adsorption on (a) PCO, (b) PNO, and (c) PZO catalysts, along with PEDA results for (d) CH_3OH–PCO, (e) CH_3OH–PNO, and (f) CH_3OH–PZO systems. Color code: Pr (purple), Cu (blue), Ni (light gray), Zn (yellow), C (gray), O (red), and H (white).

the GGA-PBEsol functional with a Slater-type DZP basis set.[69] The PEDA results indicate that methanol exhibits the strongest interaction with the PCO catalyst, with an interaction energy of −0.470 eV. In contrast, weaker interactions were observed for PNO (−0.184 eV), while PZO displayed an unfavorable interaction with a slightly positive energy of +0.036 eV. In the CH_3OH–PCO system, the dominant interaction component was Pauli repulsion (+2.281 eV), counterbalanced by substantial electrostatic (−1.860 eV) and orbital (−0.891 eV) contributions. For PNO and PZO, the orbital interactions were significantly smaller (−0.129 and −0.012 eV, respectively), and their electrostatic components were −0.128 eV (PNO) and +0.052 eV (PZO), with Pauli repulsion of +0.073 eV and −0.003 eV, respectively. Notably, the interaction within the CH_3OH–PCO system was dominated by attractive electrostatic and orbital contributions, indicating significant charge redistribution and considerable orbital overlapping. In comparison, the orbital contributions for PNO and PZO were 70.10% and 33.33%, of the total interaction energy, respectively. These findings highlight that methanol adsorption on the PCO surface induces substantial electronic rearrangement, which promotes methanol adsorption and subsequent oxidation. Overall, the PEDA results clearly establish the PCO as the most promising catalyst among the three, offering favorable energetics for methanol adsorption and dissociation into key MOR intermediates.

Building upon the aforementioned findings, the subsequent mechanistic investigation in this study focuses exclusively on the PCO catalyst, owing to its superior methanol adsorption capability and enhanced activation behavior relative to its PNO and PZO counterparts. The notable orbital interactions arising from substantial charge redistribution during methanol adsorption on PCO further affirm its promising catalytic behavior.

Catalysis

To gain deeper insights into the MOR pathway on the PCO surface, a detailed analysis of the adsorption behavior of key reaction intermediates was carried out. This allowed for a comprehensive understanding of the stepwise transformation of methanol during its electrochemical oxidation. Specifically, the dehydrogenation of methanol into CO and H_2 was found to proceed *via* four distinct mechanistic pathways, as summarized in eqn ((2)–(5)).

$$CH_3OH^* \rightarrow CH_3O^* + H^* \rightarrow CH_2O^* + H^* \rightarrow CHO^* + H^* \rightarrow CO^* + H^* \text{ (Scheme 1)} \quad (2)$$

$$CH_3OH^* \rightarrow CH_2OH^* + H^* \rightarrow CH_2O^* + H^* \rightarrow CHO^* + H^* \rightarrow CO^* + H^* \text{ (Scheme 2)} \quad (3)$$

$$CH_3OH^* \rightarrow CH_2OH^* + H^* \rightarrow CHOH^* + H^* \rightarrow CHO^* + H^* \rightarrow CO^* + H^* \text{ (Scheme 3)} \quad (4)$$

$$CH_3OH^* \rightarrow CH_2OH^* + H^* \rightarrow CHOH^* + H^* \rightarrow COH^* + H^* \rightarrow CO^* + H^* \text{ (Scheme 4)} \quad (5)$$

which further leads to the final steps where COOH* and CO_2 formation take place, as shown in eqn (6),

$$CO^* + OH^- \rightarrow COOH^* + H^* \rightarrow CO_2^* + H^* \quad (6)$$

Methanol dehydrogenation can be broadly categorized into two types: (i) reaction initiate with O–H bond cleavage (Scheme 1) and (ii) another involving initial C–H bond cleavage (Scheme 2–4) as shown in Fig. 4. The elementary reaction steps and their corresponding relative Gibbs free energy (ΔG) values are provided in the SI.

Mechanistic insights and comparative analysis of reaction pathways

The PCO catalyst exhibits superior methanol adsorption and efficient electron redistribution, attributed to strong electronic coupling between methanol and the catalyst surface, which facilitates charge transfer and enhances both catalytic activity and stability toward the MOR.

In Scheme 1, the initial O–H bond cleavage of CH_3OH forms a highly stable CH_3O^* intermediate (ΔG = −3.09 eV). However, this thermodynamic favorability comes at the cost of a higher energy barrier for the subsequent dehydrogenation of the CH_2O^* intermediate, rendering the overall pathway kinetically unfavorable.

After the initial C–H bond cleavage (Scheme 2 and 3) CH_2-OH forms and can follow two possible dehydrogenation pathways: one proceeding *via* CH_2O to CHO, and the other through CHOH to CHO. Although both routes converge at the CHO intermediate, the CH_2O pathway is more thermodynamically favorable (ΔG = −1.27 eV) than the CHOH route (ΔG = 0.58 eV), likely due to stronger CH_2O adsorption. Despite this, the CHO* intermediate in the CH_2O pathway exhibits a high relative Gibbs free energy of 1.65 eV, indicating weak adsorption and introducing a significant energetic barrier. In contrast, Scheme 3 offers a more stable CHO* intermediate (ΔG = −0.21 eV), suggesting a smoother and energetically viable route for methanol oxidation.

Scheme 4 presents a distinct and more favorable pathway. Here, CHOH is transformed into COH, followed by its dehydrogenation to CO, then COOH, and finally CO_2. The corresponding relative Gibbs free energies, CHOH (0.58 eV), COH (0.31 eV), CO (0.09 eV), COOH (−6.36 eV), and CO_2 (0.52 eV), reveal a downhill energy profile up to COOH. This not only facilitates the full oxidation of methanol but also ensures efficient desorption of CO and CO_2, mitigating catalyst poisoning and enhancing long-term performance. Overall, the comparative thermodynamic analysis identifies Scheme 4 as the most energetically favorable and practically

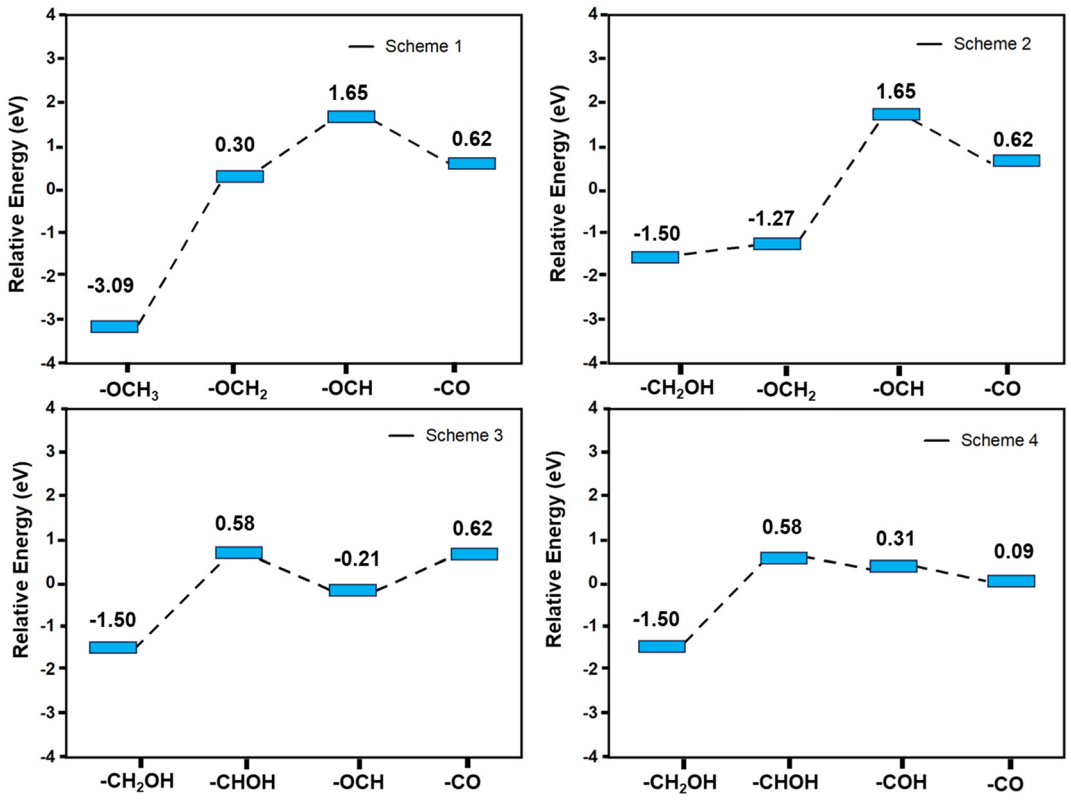

Fig. 4 Relative Gibbs free energy diagrams for the methanol oxidation reaction (MOR) calculated for four different mechanistic pathways (Scheme 1–4).

viable pathway for methanol oxidation over the PCO catalyst, due to its lower energy barriers, stable intermediate formation, and anti-poisoning characteristics.

Differential charge density analysis and adsorption energy

To further elucidate the MOR mechanism and the role of Cu atoms in the PCO catalyst, differential charge density ($\Delta\rho$) analyses were conducted at each reaction step. The differential charge density ($\Delta\rho$) was calculated using the expression $(\rho(C_{\text{PCO–intermediate}}) - \rho(C_{\text{intermediate}}) - \rho(C_{\text{PCO}}))$, where $\rho(C_{\text{PCO–intermediate}})$ represents the charge density of the catalyst with the adsorbed intermediate, $\rho(C_{\text{intermediate}})$ corresponds to the charge density of the isolated intermediate, and $\rho(C_{\text{PCO}})$ denotes the charge density of the bare PCO catalyst. This analysis highlights charge redistribution during adsorption, offering insights into electronic interactions between PCO and reaction intermediates (Fig. 5; SI and S7).

The charge density difference plots reveal a pronounced charge redistribution at the PCO–intermediate interface, indicating strong interactions across all plausible reaction pathways. In particular, Scheme 4 shows the most significant electron delocalization. The cyan and yellow regions in the plots represent electron depletion around the Cu atoms and accumulation near the adsorbed intermediates, respectively.

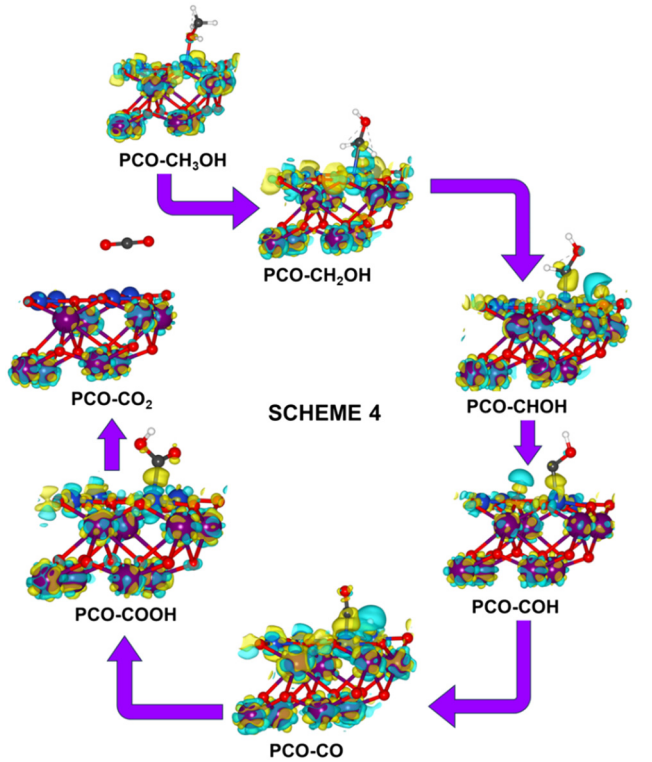

Fig. 5 Scheme 4 along with the differential charge density analyses. The cyan and yellow color represent the electron depletion and electron accumulation, respectively (isovalue 0.01 au). Color code: purple: Pr, blue: Cu, gray: C, red: O, and white: H.

This flow of electrons from Cu to the intermediates confirms a key role for Cu in mediating electron transfer, thereby enhancing catalytic performance.

Complementary to the differential charge density analysis, adsorption energy calculations were performed, further supporting that Scheme 4 represents the most favorable pathway MOR. The adsorption energy were calculated using the following equation: $(E(C_{\text{PCO–intermediate}}) - E(C_{\text{intermediate}}) - E(C_{\text{PCO}}))$, where $E(C_{\text{PCO–intermediate}})$ represents the total energy of the catalyst with the adsorbed intermediate, $E(C_{\text{intermediate}})$ corresponds to the total energy of the isolated intermediate, and $E(C_{\text{PCO}})$ denotes the total energy of the bare PCO catalyst. These calculated adsorption energies reflect the strength of intermediate binding to the catalyst surface and are presented in SI, Fig. S8.

Scheme 4 exhibits the most optimal balance between the adsorption of intermediates and their efficient desorption. Intermediates such as CHOH and COH exhibit adsorption energies of −3.61 eV and −4.85 eV, supporting their stable binding and effective progression through subsequent reaction steps. Notably, CO exhibits a moderate adsorption energy (−1.72 eV), which facilitates its timely desorption and mitigates surface poisoning. Favorable adsorption of COOH and CO_2 further supports continuous catalytic turnover.

The correlation between adsorption energies and the relative Gibbs free energy profile confirms Scheme 4 as the most thermodynamically and kinetically viable pathway for methanol oxidation over the PCO catalyst. Collectively, the relative Gibbs free energy profile, differential charge density analysis, and adsorption energy shows that Scheme 4 as the most efficient and energetically favorable route for MOR on the PCO surface.

Electronic properties

The PCO catalyst exhibits metallic characteristics, as confirmed by a pronounced electron density at the Fermi level. The projected density of states (PDOS), shown in Fig. 6 reveals significant orbital overlap between the Cu^{2+} (t_{2g} and e_g) 3d states and the O 2p orbitals in the valence band. This strong hybridization originates from the spatial proximity between Cu^{2+} centers and equatorial oxygen atoms, facilitating covalent Cu–O bonding. As a result, the Fermi level becomes pinned near the top of the O 2p band, contributing to improved electronic conductivity and catalytic activity. The presence of Cu 3d orbitals at the Fermi level also reduces the number of occupied antibonding states below it, which enhances the adsorption strength of reaction intermediates and supports their stability during the MOR. In addition, a notable contribution from Pr 4f orbitals at the Fermi level further boosts the intrinsic electronic conductivity of PCO. The interaction between Cu 3d, Pr 4f, and O 2p orbitals minimizes charge-transfer resistance and facilitates efficient electron mobility, an essential factor for promoting MOR kinetics.

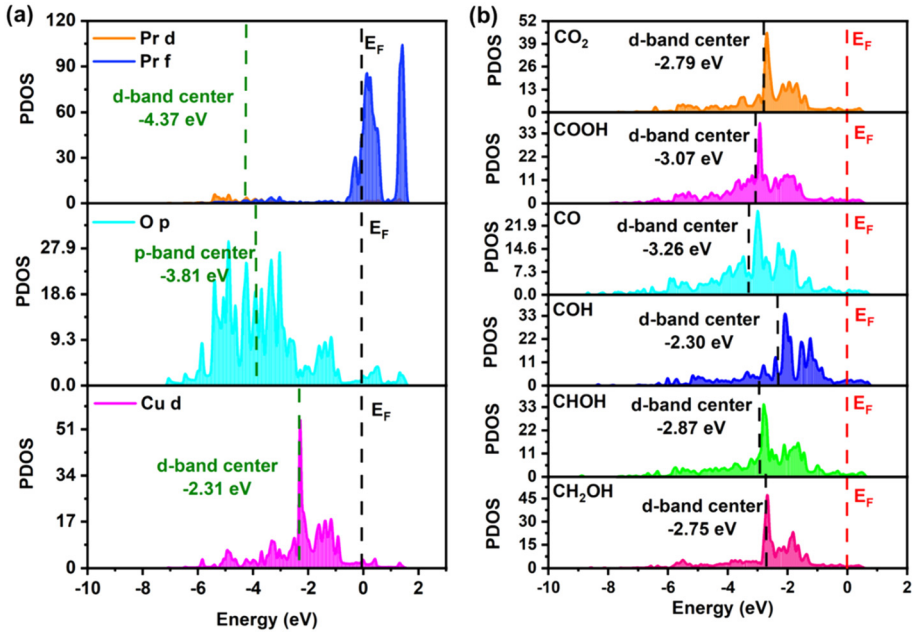

Fig. 6 PDOS of (a) PCO catalyst along with the d-band center and (b) d-band center of Cu during the adsorption of intermediates involving Scheme 4.

Although Pr 4f electrons are largely localized and shielded, their indirect role in modulating the electronic structure of Cu sites is significant. Through intra-atomic 4f–5d–6s coupling, the unpaired 4f electrons induce surface spin polarization, altering the local electronic environment around Cu^{2+} and increasing Cu 3d–O 2p hybridization.[70,71] This effect enhances electron delocalization and accelerates charge transfer processes. Furthermore, the d–f orbital coupling across the Cu–O–Pr network enables directional electron transport, improving catalytic turnover and intermediate conversion. These findings are in strong agreement with recent studies highlighting the importance of 4f orbitals in enhancing conductivity, charge transfer efficiency, and electrocatalytic activity during MOR.[70,71]

Various high-performance catalysts have been identified through computational analysis, a deeper understanding of the correlation between catalyst structure and catalytic behavior remains crucial for the rational design of more efficient electrocatalysts.[70–72] The d-band center theory, in conjunction with Sabatier's principle, serves as a powerful framework for explaining catalytic activity.[72] According to this theory, a d-band center located near the Fermi level typically corresponds to stronger interactions between the catalyst surface and adsorbed species, enhancing catalytic performance.[72] However, optimal activity is generally achieved when the d-band center maintains a moderate position *i.e.* not too close to, nor too far from, the Fermi level.[72]

Fig. 6 illustrates the variation in d-band center of Cu before and after intermediate adsorption, with particular emphasis on Scheme 4, the most energetically favorable pathway for methanol oxidation. For comparison, the d-band center shifts associated with intermediates in Scheme 1–3 are also analyzed and presented in SI, Fig. S9. Notably, the d-band center of Cu in the PCO catalyst is found to be moderately positioned relative to the Fermi level, striking an effective balance between adsorption and desorption of intermediates, which supports its high catalytic efficiency. In addition to favorable adsorption behavior, the catalytic activity of PCO is also influenced by electronic properties at the active sites, including increased charge density and efficient electron transfer. The electronic properties further corroborate the superior performance of the PCO catalyst in facilitating methanol electrooxidation.

Experimental validation of superior methanol oxidation activity of PCO compared to PNO and PZO catalysts

The enhanced MOR performance of the PCO catalyst, as revealed by theoretical analyses, can be attributed to its stronger methanol–surface interaction and more favorable electronic structure compared to PNO and PZO. Furthermore, the catalytic performance during MOR is also significantly influenced by factors such as material composition, morphology, porosity, and surface area, all of which affect methanol accessibility to active sites. These parameters, in turn, impact the resulting current density during electrochemical oxidation. Thus, to evaluate the electrocatalytic performance, a series of cyclic voltammetry (CV) measurements were performed in acidic media, as shown in Fig. 7. The synthesized nanocatalysts, PCO, PNO, and PZO, were tested in an electrolyte containing 0.5 M H_2SO_4 and varying concentrations of CH_3OH (0.2–1 M) at a scan rate of 50 mV s^{-1}. Among the three catalysts, only PCO

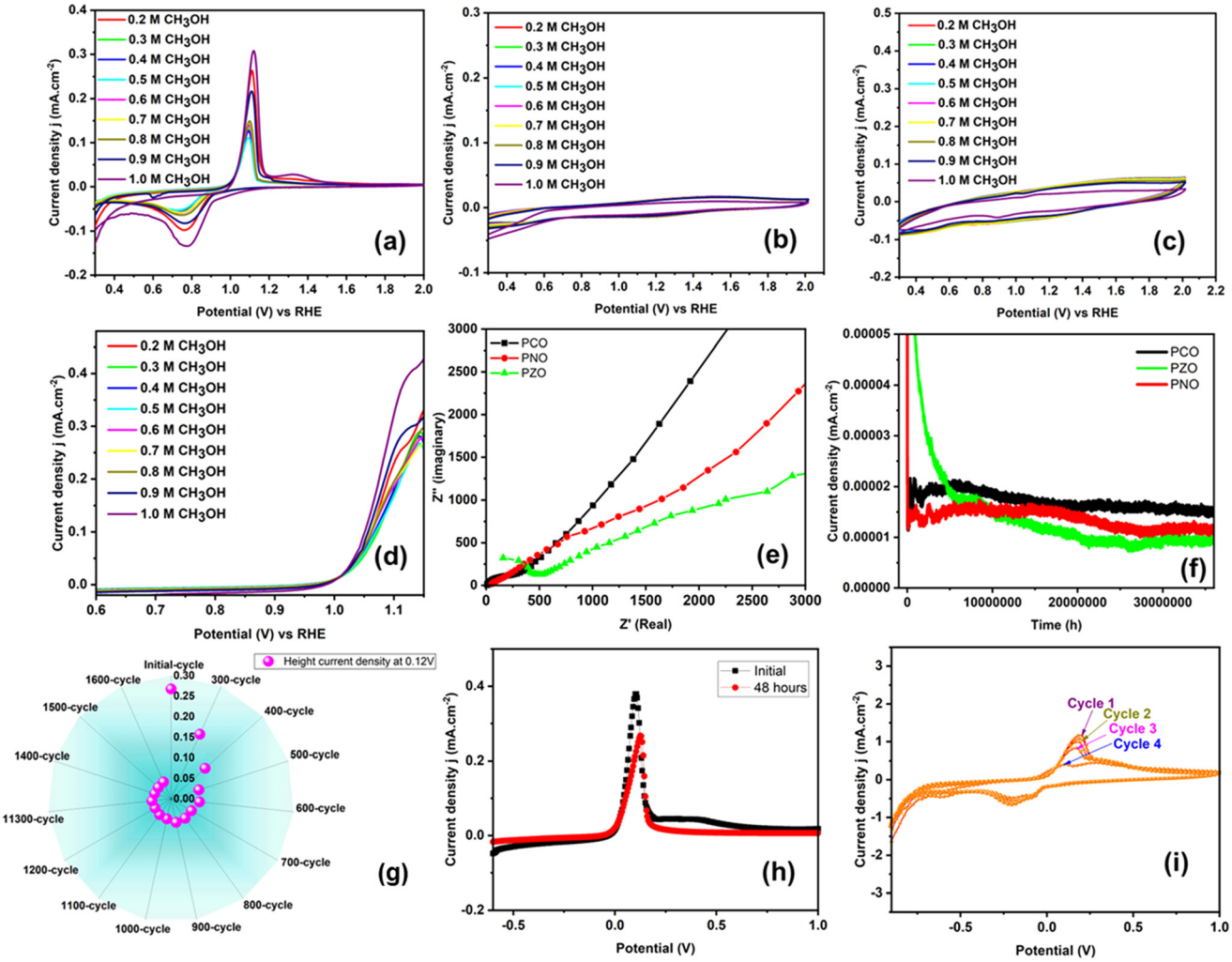

Fig. 7 (a–c) CV plot at various concentration (0.2–1.0 M) of CH_3OH solution + 0.5 M H_2SO_4 at a scan rate of 50 mV s^{-1} *versus* the RHE for PCO, PNO, and PZO respectively, (d) LSV plot at concentration of CH_3OH solution + 0.5 M H_2SO_4 at a scan rate of 50 mV s^{-1} *versus* the RHE for PCO, (e) Nyquist plot, (f) chronoamperometry (*I*–*t* measurements) in 0.5 M H_2SO_4, (g) continuous 1600-cycle CV test of the PCO catalyst in a 0.5 M CH_3OH + 0.5 M H_2SO_4 solution at a scan rate of 100 mV s^{-1}, (h) comparison of the current densities between the initial cycle and after 48 hours of CV cycling under the same conditions, (i) CO-stripping analysis for PCO catalyst.

exhibited a distinct oxidation response, evidenced by a well-defined anodic peak at approximately 1.09 V *vs.* RHE with a corresponding current density of 0.10 mA cm^{-2} in 0.5 M CH_3-OH + 0.5 M H_2SO_4. As shown in Fig. 7a and d, the MOR peak current density varies non-linearly with methanol concentration. The current decreases as the concentration increases from 0.2 to 0.3 M. It then remains nearly constant between 0.5 and 0.7 M, as the catalyst surface reaches a dynamic equilibrium between adsorption and desorption of intermediates. At higher concentrations, up to 1.0 M, the abundant methanol supply overcomes earlier transport limitations and ensures sufficient reactant flux to the catalytic surface. This behaviour arises from the combined effects of reactant availability, surface dynamics, and mass-transport limitations.

In contrast, PNO and PZO showed no observable oxidation peaks under identical conditions, confirming their inactivity toward MOR. The CV profile of PCO featured two prominent anodic peaks: a forward peak (I_a) corresponding to the electrooxidation of methanol on the oxide-modified electrode surface, and a reverse peak (I_b), attributed to the intermediates accumulated during the forward scan. This anodic hysteresis further supports the active involvement of surface-bound intermediates during the catalytic cycle. These electrochemical findings strongly support the theoretical predictions and underscore the superior MOR activity of the PCO catalyst over its PNO and PZO counterparts.

Linear sweep voltammetry (LSV) further corroborated the superior MOR performance of the PCO catalyst. As shown in Fig. 7d, PCO exhibited an onset potential of ~0.96 V *vs.* RHE for MOR, whereas no discernible oxidation peaks were detected for PNO and PZO (SI, Fig. S10), emphasizing the high selectivity of PCO. LSV measurements were conducted in 0.5 M H_2SO_4 with varying CH_3OH concentrations (0.2–1

M), reinforcing the robust activity of PCO. CV analyses at scan rates from 10 to 300 mV s^{-1} in 0.5 M H_2SO_4 + 0.5 M CH_3OH (SI, Fig. S11(a–c)) revealed a linear increase in both anodic and cathodic current densities with increasing scan rate, indicating diffusion-controlled electrochemical behavior.

Electrochemical impedance spectroscopy (EIS) was employed to evaluate the charge transfer characteristics of the catalysts (Fig. 7e). The Nyquist plot of PCO revealed a small semicircle, indicative of low charge transfer resistance (R_{ct}) of 10.41 Ω, in contrast to PNO (17.85 Ω) and PZO (79.01 Ω), demonstrating the superior electron transport capabilities of PCO. The equivalent circuit models used for fitting the EIS data are provided in SI, Fig. S12. Additionally, the calculated theoretical onset potential (~0.09 V) closely aligns with the experimental value (~0.05 V), lending further credence to Scheme 4 as the most favorable reaction pathway for MOR on PCO.

Durability tests confirmed the long-term electrochemical stability of the PCO catalyst. The CA measurements, performed in 0.5 M H_2SO_4 without methanol, assessed the stability of the catalyst layer under a constant potential of 0.5 V over 10 hours (Fig. 7f) and showed a sustained current density. In addition, CV cycling at 100 mV s^{-1} for 500 cycles in 0.5 M H_2SO_4 + 0.5 M CH_3OH (SI, Fig. S13) demonstrated negligible degradation of the catalyst. Extended stability was also verified over 1600 CV cycles at 100 mV s^{-1} (Fig. 7g). A gradual decrease in current density was observed with an increasing cycle number. This attenuation is primarily attributed to temporary surface passivation, arising from the accumulation of reaction intermediates (*e.g.*, CO, and CH_xO species) that adsorb onto active sites and inhibit further methanol oxidation. To probe the nature of this performance loss, the same electrode was reused after 48 hours in a fresh electrolyte (0.5 M H_2SO_4 + 0.5 M CH_3OH), as depicted in Fig. 7h. The resulting CV curve exhibited only marginal variation in current density, with no significant change in the anodic peak position or intensity compared to the initial cycle. This recovery confirms that the observed performance degradation was not due to catalyst decomposition, but rather due to electrolyte consumption. Upon electrolyte renewal, the adsorbed intermediates were effectively oxidized, re-exposing active sites and restoring catalytic performance.

The PCO catalyst also demonstrated exceptional mass activity (M_A), measured at 0.75 A mg^{-1}, which is significantly higher than that of several benchmark Pt-based catalysts, such as $Pt_{62}Ru_{35}$/C (0.47 A mg^{-1}),[73] $Pt_{62}Ru_{18}Ni_{20}$-O/C (0.30 A mg^{-1}),[73] and PtZn intermetallic nanoparticles (0.58 A mg^{-1}).[74] Detailed M_A calculations and comparative data are provided in the SI, Table S2. Collectively, these findings establish PCO as a highly efficient and stable catalyst for methanol oxidation in acidic media. Its favorable electronic structure, low charge transfer resistance, and outstanding durability outperform conventional Pt-based systems, making it a promising non-precious alternative for future energy conversion technologies.

CO-stripping analysis

To assess the anti-poisoning capability of the PCO catalyst, CO-stripping voltammetry was performed, as shown in Fig. 7i. A distinct CO oxidation peak was observed during the initial cycles, followed by a substantial reduction in peak intensity with subsequent scans, indicating effective CO oxidation and removal from the catalyst surface. Notably, the low onset potential of ~0.05 V signifies the catalyst's exceptional tolerance to CO poisoning.

To corroborate these observations, complementary characterization techniques, including ^{13}C-NMR and ^{1}H-NMR spectroscopy, were employed. The absence of C and C–H related peaks in the post-electrocatalysis spectra (SI, Fig. S14 and S15) strongly indicates effective CO desorption from the PCO catalyst surface. This efficient desorption process significantly minimizes CO poisoning, as further validated by the supporting data presented in SI, Fig. S14 and S15. Moreover, ^{13}C-NMR and ^{1}H-NMR analyses of the liquid electrolyte after methanol oxidation confirmed the complete conversion of CH_3OH to CO_2, with no detectable by-products. These findings demonstrate that the PCO catalyst exhibits exceptional resistance to CO poisoning, a crucial attribute for maintaining catalytic activity and stability during methanol oxidation. The catalyst's ability to prevent CO adsorption and promote its complete oxidation to CO_2 underscores its potential as a durable and efficient candidate for methanol oxidation reactions in acidic media.

Post-electrocatalysis XRD confirmed the retention of the PCO phase with minor shift in the peak position, while FTIR revealed characteristic Pr–O vibrations along with a new band at ~505 cm^{-1}, indicating marginal structural modifications associated with Cu–O(II) linkages. Detail discussion is provided in SI, Fig. S16. Overall, the PCO catalyst demonstrates high stability and resistance to CO poisoning during methanol oxidation, with post-electrocatalysis analyses confirming retention of the crystalline phase with small structural modifications.

Conclusion

Praseodymium-based mixed oxides (PCO, PNO, and PZO) were systematically synthesized and characterized to evaluate their potential as electrocatalysts for methanol oxidation. Structural and spectroscopic analyses confirmed the formation of single-phase, porous nanostructures with well-distributed Pr, M (Cu/Ni/Zn), and O elements. Among them, PCO exhibited the highest surface area and strongest Cu–O–Pr interactions, providing a favorable framework for catalytic activity. PEDA confirmed that PCO exhibits the most favorable adsorption energetics (−0.470 eV), where strong electrostatic and orbital interactions contribute to efficient methanol binding and subsequent catalytic turnover, while PNO and PZO showed weaker or even unfavorable adsorption characteristics. In addition, DFT calculations further revealed that PCO offers the most stable methanol adsorption and an energetically favorable C–H bond

cleavage pathway, with Cu sites playing a central role in electron transfer and CO oxidation. The electronic properties and d-band analyses indicated metallic behavior with strong Cu 3d–O 2p–Pr 4f hybridization, which enhances electronic conductivity, stabilizes key intermediates, and prevents CO poisoning.

Electrochemical studies validated these theoretical predictions, demonstrating that PCO exhibits the lowest onset potential (~0.96 V *vs.* RHE), highest peak current density (~0.10 mA cm^{-2}), and superior CO tolerance compared to PNO and PZO. EIS confirmed the lowest charge-transfer resistance for PCO (10.41 Ω), while durability and CO-stripping tests established excellent stability and complete methanol conversion to CO_2 without any by-products. The mass activity of PCO (0.75 A mg^{-1}) even surpasses several Pt-based benchmarks, underscoring its promise as a cost-effective and earth-abundant MOR catalyst. Overall, this integrated experimental and theoretical study establishes PCO as the most efficient among the investigated Pr-based oxides and highlights the importance of 4f–3d–2p electronic interactions in designing advanced electrocatalysts for direct alcohol fuel cells. Future research may focus on dopant engineering, heterostructure formation, or composite hybridization to further improve catalytic performance and broaden the scope of application in sustainable energy conversion technologies.

Conflicts of interest

The authors declare no competing financial interest.

Data availability

All the data support the findings of article is provided in electronic supplementary information (SI). Supplementary information: the detailed experimental and theoretical methodology used in the present investigation is provided in materials and method section, EDS, XPS, and XRD analysis, electro-oxidation of methanol, optimized geometry, elementary steps in the MOR involving electron transfer, along with their corresponding reaction free energy expressions and their electronic properties, CV analysis, ^{13}C NMR, ^{1}H-NMR, and comparison between the synthesized catalyst with other Pt-based nano-catalyst. See DOI: **https://doi.org/10.1039/d5re00313j**.

Acknowledgements

We are thankful to funding agency DST-SERB (EEQ/2023/000424, ECR/2018/002346 and EEQ/2019/000656) Delhi, India for proving the financial support. We are also thankful to the Director, National Institute of Technology Warangal for providing the facilities. One of the authors Pooja also thankful to the Ministry of Education (MoE), formerly the Ministry of Human Resource Development (MHRD) for providing Senior Research Fellowship (SRF). We would also like to thank IIT Kanpur for providing the XPS facility, IIT-ISM Dhanbad for the HRTEM facility, and NIT Warangal for the FESEM, and XRD facilities. We acknowledge National Supercomputing Mission (NSM) for providing computing resources of 'PARAM Himalaya' at IIT Mandi, which is implemented by C-DAC and supported by the Ministry of Electronics and Information Technology (MeitY) and Department of Science and Technology (DST), Government of India.

References

1 C. Sun, R. Hui and J. Roller, Cathode Materials for Solid Oxide Fuel Cells: A Review, *J. Solid State Electrochem.*, 2010, **14**(7), 1125–1144, DOI: **10.1007/s10008-009-0932-0**.

2 A. M. Abdalla, S. Hossain, A. T. Azad, P. M. I. Petra, F. Begum, S. G. Eriksson and A. K. Azad, Nanomaterials for Solid Oxide Fuel Cells: A Review, *Renewable Sustainable Energy Rev.*, 2018, **82**, 353–368, DOI: **10.1016/j.rser.2017.09.046**.

3 D. Lee and H. N. Lee, Controlling Oxygen Mobility in Ruddlesden–Popper Oxides, *Materials*, 2017, **10**(4), 368, DOI: **10.3390/ma10040368**.

4 D. J. L. Brett, A. Atkinson, N. P. Brandon and S. J. Skinner, Intermediate Temperature Solid Oxide Fuel Cells, *Chem. Soc. Rev.*, 2008, **37**(8), 1568–1578, DOI: **10.1039/B612060C**.

5 H. Zhao, Q. Li and L. Sun, Ln2MO4 Cathode Materials for Solid Oxide Fuel Cells, *Sci. China:Chem.*, 2011, **54**(6), 898–910, DOI: **10.1007/s11426-011-4290-2**.

6 J. C. Grenier, F. Mauvy, C. Lalanne, J.-M. Bassat, F. Chauveau, J. Mougin, J. Dailly and M. Marrony, A2MO4+δ Oxides: Flexible Electrode Materials for Solid Oxide Cells, *ECS Trans.*, 2009, **25**(2), 2537, DOI: **10.1149/1.3205810**.

7 M. Al Daroukh, V. V. Vashook, H. Ullmann, F. Tietz and I. Arual Raj, Oxides of the AMO3 and A2MO4-Type: Structural Stability, Electrical Conductivity and Thermal Expansion, *Solid State Ionics*, 2003, **158**(1), 141–150, DOI: **10.1016/S0167-2738(02)00773-7**.

8 A. P. Tarutin, J. G. Lyagaeva, D. A. Medvedev, L. Bi and A. A. Yaremchenko, Recent Advances in Layered Ln2NiO4+δ Nickelates: Fundamentals and Prospects of Their Applications in Protonic Ceramic Fuel and Electrolysis Cells, *J. Mater. Chem. A*, 2021, **9**(1), 154–195, DOI: **10.1039/D0TA08132A**.

9 V. Venkataraman, M. Pérez-Fortes, L. Wang, Y. S. Hajimolana, C. Boigues-Muñoz, A. Agostini, S. J. McPhail, F. Maréchal, J. Van Herle and P. V. Aravind, Reversible Solid Oxide Systems for Energy and Chemical Applications – Review & Perspectives, *J. Energy Storage*, 2019, **24**, 100782, DOI: **10.1016/j.est.2019.100782**.

10 G. Yang, C. Su, H. Shi, Y. Zhu, Y. Song, W. Zhou and Z. Shao, Toward Reducing the Operation Temperature of Solid Oxide Fuel Cells: Our Past 15 Years of Efforts in Cathode Development, *Energy Fuels*, 2020, **34**(12), 15169–15194, DOI: **10.1021/acs.energyfuels.0c01887**.

11 M. Liu, R. Peng, D. Dong, J. Gao, X. Liu and G. Meng, Direct Liquid Methanol-Fueled Solid Oxide Fuel Cell, *J. Power*

Sources, 2008, **185**(1), 188–192, DOI: **10.1016/j.jpowsour.2008.06.076**.

12 T. Kim, K. Ahn, J. M. Vohs and R. J. Gorte, Deactivation of Ceria-Based SOFC Anodes in Methanol, *J. Power Sources*, 2007, **164**(1), 42–48, DOI: **10.1016/j.jpowsour.2006.09.101**.

13 D. Y. Jang, J. Koo, H. R. Choi, J. W. Kim, H. J. Jeong, F. B. Prinz and J. H. Shim, Coke-Free Oxidation of Methanol in Solid Oxide Fuel Cells with Heterogeneous Nickel–Palladium Catalysts Prepared by Atomic Layer Deposition, *ACS Sustainable Chem. Eng.*, 2020, **8**(28), 10529–10535, DOI: **10.1021/acssuschemeng.0c03020**.

14 J. Byeon, S. Kim, S. Lee, J. H. Jang, S.-K. Kim and J. Lee, CO-Tolerant Electrocatalysts for Hydrogen Fuel Cells: Fundamental Study-Based Design and Real-Life Applications, *Chem. Eng. J.*, 2024, **493**, 152626, DOI: **10.1016/j.cej.2024.152626**.

15 W. Luo, Y. Jiang, M. Wang, D. Lu, X. Sun and H. Zhang, Design Strategies of Pt-Based Electrocatalysts and Tolerance Strategies in Fuel Cells: A Review, *RSC Adv.*, 2023, **13**(7), 4803–4822, DOI: **10.1039/D2RA07644F**.

16 L. Huang, S. Zaman, X. Tian, Z. Wang, W. Fang and B. Y. Xia, Advanced Platinum-Based Oxygen Reduction Electrocatalysts for Fuel Cells, *Acc. Chem. Res.*, 2021, **54**(2), 311–322, DOI: **10.1021/acs.accounts.0c00488**.

17 X. Ren, Q. Lv, L. Liu, B. Liu, Y. Wang, A. Liu and G. Wu, Current Progress of Pt and Pt-Based Electrocatalysts Used for Fuel Cells, *Sustainable Energy Fuels*, 2019, **4**(1), 15–30, DOI: **10.1039/C9SE00460B**.

18 Z. Wei, S. Yu and C. Li, Research Development of Anti-CO Poisoning in Electrocatalytic Methanol Oxidation Processes: A Review, *Catal. Sci. Technol.*, 2024, **14**(18), 5128–5142, DOI: **10.1039/D4CY00726C**.

19 J. Solla-Gullón, F. J. Vidal-Iglesias and J. M. Feliu, Shape Dependent Electrocatalysis, *Annu. Rep. Prog. Chem., Sect. C: Phys. Chem.*, 2011, **107**(0), 263–297, DOI: **10.1039/C1PC90010B**.

20 B. Marzougui, A. Marzouki, Y. B. Smida, R. Marzouki, B. Marzougui, A. Marzouki, Y. B. Smida and R. Marzouki, The Cuprate Ln_2CuO_4 (Ln: Rare Earth): Synthesis, Crystallography, and Applications. in *Crystal Growth and Chirality - Technologies and Applications*, IntechOpen, 2023, DOI: **10.5772/intechopen.109193**.

21 K. A. Müller, The Unique Properties of Superconductivity in Cuprates, *J. Supercond. Novel Magn.*, 2014, **27**(10), 2163–2179, DOI: **10.1007/s10948-014-2751-5**.

22 L. M. Kolchina, N. V. Lyskov, P. P. Pestrikov, S. Y. Istomin, G. N. Mazo and E. V. Antipov, Evaluation of La1.8−xPrxSr0.2CuO4−δ Oxides as Cathode Materials for IT-SOFCs, *Mater. Chem. Phys.*, 2015, **165**, 91–96, DOI: **10.1016/j.matchemphys.2015.08.059**.

23 K. Zheng, A. Gorzkowska-Sobaś and K. Świerczek, Evaluation of Ln2CuO4 (Ln: La, Pr, Nd) Oxides as Cathode Materials for IT-SOFCs, *Mater. Res. Bull.*, 2012, **47**(12), 4089–4095, DOI: **10.1016/j.materresbull.2012.08.072**.

24 E. Boehm, J.-M. Bassat, P. Dordor, F. Mauvy, J.-C. Grenier and P. Stevens, Oxygen Diffusion and Transport Properties in Non-Stoichiometric Ln2 − xNiO4 + δ Oxides, *Solid State Ionics*, 2005, **176**(37), 2717–2725, DOI: **10.1016/j.ssi.2005.06.033**.

25 L. Li, J. Zhou, Z. Hu, S. Choi, G. Kim, J.-Q. Wang and L. Zhang, First-Principles Insight into the Effects of Intrinsic Oxygen Defects on Proton Conduction in Ruddlesden–Popper Oxides, *J. Phys. Chem. Lett.*, 2021, **12**(47), 11503–11510, DOI: **10.1021/acs.jpclett.1c02749**.

26 X. Ding, X. Kong, X. Wang, J. Jiang and C. Cui, Characterization and Optimization of Ln1.7Sr0.3CuO4 (Ln = La, Nd)-Based Cathodes for Intermediate Temperature Solid Oxide Fuel Cells, *J. Alloys Compd.*, 2010, **502**(2), 472–476, DOI: **10.1016/j.jallcom.2010.04.199**.

27 Pooja and R. Pawar, Understanding Methanol Electro-Oxidation Pathways on Nd-Based Metal Oxides via DFT and Electrochemical Studies, *Langmuir*, 2025, **41**(25), 16203–16215, DOI: **10.1021/acs.langmuir.5c01441**.

28 A. P. Tarutin, M. Y. Gorshkov, I. N. Bainov, G. K. Vdovin, A. I. Vylkov, J. G. Lyagaeva and D. A. Medvedev, Barium-Doped Nickelates Nd2−xBaxNiO4+δ as Promising Electrode Materials for Protonic Ceramic Electrochemical Cells, *Ceram. Int.*, 2020, **46**(15), 24355–24364, DOI: **10.1016/j.ceramint.2020.06.217**.

29 J. Wang, C. Cheng, B. Huang, J. Cao, L. Li, Q. Shao, L. Zhang and X. Huang, Grain-Boundary-Engineered La2CuO4 Perovskite Nanobamboos for Efficient CO2 Reduction Reaction, *Nano Lett.*, 2021, **21**(2), 980–987, DOI: **10.1021/acs.nanolett.0c04004**.

30 Y. Gu, Y. Zhang, Y. Zheng, H. Chen, L. Ge and L. Guo, PrBaMn2O5+δ with Praseodymium Oxide Nano-Catalyst as Electrode for Symmetrical Solid Oxide Fuel Cells, *Appl. Catal., B*, 2019, **257**, 117868, DOI: **10.1016/j.apcatb.2019.117868**.

31 S. Sengodan, S. Choi, A. Jun, T. H. Shin, Y.-W. Ju, H. Y. Jeong, J. Shin, J. T. S. Irvine and G. Kim, Layered Oxygen-Deficient Double Perovskite as an Efficient and Stable Anode for Direct Hydrocarbon Solid Oxide Fuel Cells, *Nat. Mater.*, 2015, **14**(2), 205–209, DOI: **10.1038/nmat4166**.

32 A. P. Tarutin, A. R. Gilev, S. A. Baratov, G. K. Vdovin and D. A. Medvedev, Ba-Doped Pr2NiO4+δ Electrodes for Proton-Conducting Electrochemical Cells. Part 3: Electrochemical Applications, *Int. J. Hydrogen Energy*, 2024, **60**, 261–271, DOI: **10.1016/j.ijhydene.2024.02.173**.

33 A. R. Gilev, K. S. Sukhanov, E. A. Kiselev, M. E. Sobol and V. A. Cherepanov, Increasing Thermodynamic Stability and Electrochemical Performance of IT-SOFC Cathodes Based on Ln2MO4 (Ln = La, Pr; M = Ni, Cu), *Ceram. Int.*, 2024, **50**(20, Part C), 40453–40463, DOI: **10.1016/j.ceramint.2024.04.176**.

34 Y. Borchert, P. Sonström, M. Wilhelm, H. Borchert and M. Bäumer, Nanostructured Praseodymium Oxide: Preparation, Structure, and Catalytic Properties, *J. Phys. Chem. C*, 2008, **112**(8), 3054–3063, DOI: **10.1021/jp0768524**.

35 F. M. Aquino, D. M. A. Melo, P. M. Pimentel, R. M. Braga, M. A. F. Melo, A. E. Martinelli and A. F. Costa, Characterization and Thermal Behavior of PrMO3 (M = Co or Ni) Ceramic Materials Obtained from Gelatin, *Mater. Res.*

Bull., 2012, **47**(9), 2605–2609, DOI: **10.1016/j.materresbull.2012.04.078**.

36 B. Matović, J. Pantić, M. Prekajski, N. Stanković, D. Bučevac, T. Minović and M. Čebela, Synthesis and Characterization of Pr6O11 Nanopowders, *Ceram. Int.*, 2013, **39**(3), 3151–3155, DOI: **10.1016/j.ceramint.2012.09.098**.

37 Y. Wang, T. S. Nguyen, C. Wang and X. Wang, Ethanol Electrooxidation on Pt/C Catalysts Promoted with Praseodymium Oxide Nanorods, *Dalton Trans.*, 2009, 7606–7609, DOI: **10.1039/B909324A**.

38 J. Bak, H. Bin Bae and S.-Y. Chung, Atomic-Scale Perturbation of Oxygen Octahedra via Surface Ion Exchange in Perovskite Nickelates Boosts Water Oxidation, *Nat. Commun.*, 2019, **10**(1), 2713, DOI: **10.1038/s41467-019-10838-1**.

39 R. Jacobs, J. Hwang, Y. Shao-Horn and D. Morgan, Assessing Correlations of Perovskite Catalytic Performance with Electronic Structure Descriptors, *Chem. Mater.*, 2019, **31**(3), 785–797, DOI: **10.1021/acs.chemmater.8b03840**.

40 H. You, S. Yang, B. Ding and H. Yang, Synthesis of Colloidal Metal and Metal Alloy Nanoparticles for Electrochemical Energy Applications, *Chem. Soc. Rev.*, 2013, **42**(7), 2880–2904, DOI: **10.1039/C2CS35319A**.

41 Pooja and R. Pawar, Unveiling the Geometrical and Mechanical Properties of Σ3 (111) Grain Boundaries in Ni-Based Alloys: From Interfacial Insights, *Mater. Today Commun.*, 2024, **40**, 109469, DOI: **10.1016/j.mtcomm.2024.109469**.

42 W. Niu, Z. Chen, W. Guo, W. Mao, Y. Liu, Y. Guo, J. Chen, R. Huang, L. Kang, Y. Ma, Q. Yan, J. Ye, C. Cui, L. Zhang, P. Wang, X. Xu and B. Zhang, Pb-Rich Cu Grain Boundary Sites for Selective CO-to-n-Propanol Electroconversion, *Nat. Commun.*, 2023, **14**(1), 4882, DOI: **10.1038/s41467-023-40689-w**.

43 Pooja, R. Mucherla and R. Pawar, Envisioning the Hydrogen Dissociation in Σ5 (100) Grain Boundary in Diamond, *Diamond Relat. Mater.*, 2023, **138**, 110222, DOI: **10.1016/j.diamond.2023.110222**.

44 B. Peng, X.-Y. Chen, Y.-X. Xie, R. Shu, L.-J. Shi, H.-J. Guo, F.-P. Cheng and Q. Yi, Grain-Boundary-Enriched Copper Electrocatalysts for Efficient Carbon Dioxide Reduction to Multi-Carbon Products, *Ind. Eng. Chem. Res.*, 2025, **64**(25), 12452–12462, DOI: **10.1021/acs.iecr.5c00765**.

45 Pooja and R. Pawar, Atomistic Simulations of ∑3 [110](111) Grain Boundary in Diamond: Structure, Stability, and Properties, *Int. J. Quantum Chem.*, 2023, **123**(2), e27016, DOI: **10.1002/qua.27016**.

46 Z. Chen, T. Wang, B. Liu, D. Cheng, C. Hu, G. Zhang, W. Zhu, H. Wang, Z.-J. Zhao and J. Gong, Grain-Boundary-Rich Copper for Efficient Solar-Driven Electrochemical CO2 Reduction to Ethylene and Ethanol, *J. Am. Chem. Soc.*, 2020, **142**(15), 6878–6883, DOI: **10.1021/jacs.0c00971**.

47 Pooja, R. Mucherla and R. Pawar, Effect of Dopants on Σ3 (111) Grain Boundary in Diamond, *Phys. Status Solidi B*, 2024, **261**(1), 2300279, DOI: **10.1002/pssb.202300279**.

48 X. Feng, K. Jiang, S. Fan and M. W. Kanan, Grain-Boundary-Dependent CO2 Electroreduction Activity, *J. Am. Chem. Soc.*, 2015, **137**(14), 4606–4609, DOI: **10.1021/ja5130513**.

49 Pooja and R. Pawar, A Comprehensive Investigation of Kingery Type Σ3 (111) Grain Boundaries in TiC, TaC, and WC, *Acta Mater.*, 2024, **277**, 120168, DOI: **10.1016/j.actamat.2024.120168**.

50 L. Bian, Z.-Y. Zhang, H. Tian, N.-N. Tian, Z. Ma and Z.-L. Wang, Grain Boundary-Abundant Copper Nanoribbons on Balanced Gas-Liquid Diffusion Electrodes for Efficient CO2 Electroreduction to C2H4, *Chin. J. Catal.*, 2023, **54**, 199–211, DOI: **10.1016/S1872-2067(23)64540-1**.

51 P. E. Blöchl, Projector Augmented-Wave Method, *Phys. Rev. B: Condens. Matter Mater. Phys.*, 1994, **50**(24), 17953–17979, DOI: **10.1103/PhysRevB.50.17953**.

52 G. Kresse and J. Furthmüller, Efficient Iterative Schemes for Ab Initio Total-Energy Calculations Using a Plane-Wave Basis Set, *Phys. Rev. B: Condens. Matter Mater. Phys.*, 1996, **54**(16), 11169–11186, DOI: **10.1103/PhysRevB.54.11169**.

53 G. Kresse and J. Furthmüller, Efficiency of Ab-Initio Total Energy Calculations for Metals and Semiconductors Using a Plane-Wave Basis Set, *Comput. Mater. Sci.*, 1996, **6**(1), 15–50, DOI: **10.1016/0927-0256(96)00008-0**.

54 J. P. Perdew, A. Ruzsinszky, G. I. Csonka, O. A. Vydrov, G. E. Scuseria, L. A. Constantin, X. Zhou and K. Burke, Restoring the Density-Gradient Expansion for Exchange in Solids and Surfaces, *Phys. Rev. Lett.*, 2008, **100**(13), 136406, DOI: **10.1103/PhysRevLett.100.136406**.

55 J. P. Perdew, K. Burke and M. Ernzerhof, Generalized Gradient Approximation Made Simple, *Phys. Rev. Lett.*, 1996, **77**(18), 3865–3868, DOI: **10.1103/PhysRevLett.77.3865**.

56 H. J. Monkhorst and J. D. Pack, Special Points for Brillouin-Zone Integrations, *Phys. Rev. B: Solid State*, 1976, **13**(12), 5188–5192, DOI: **10.1103/PhysRevB.13.5188**.

57 J. K. Nørskov, J. Rossmeisl, A. Logadottir, L. Lindqvist, J. R. Kitchin, T. Bligaard and H. Jónsson, Origin of the Overpotential for Oxygen Reduction at a Fuel-Cell Cathode, *J. Phys. Chem. B*, 2004, **108**(46), 17886–17892, DOI: **10.1021/jp047349j**.

58 J. K. Nørskov, T. Bligaard, B. Hvolbæk, F. Abild-Pedersen, I. Chorkendorff and C. H. Christensen, The Nature of the Active Site in Heterogeneous Metal Catalysis, *Chem. Soc. Rev.*, 2008, **37**(10), 2163–2171, DOI: **10.1039/B800260F**.

59 H. Y. Hwang, S.-W. Cheong, A. S. Cooper, L. W. Rupp, B. Batlogg, G. H. Kwei and Z. Tan, Crystallographic Evolution, T′→T*→T,in Pr2−xSrxCuO4−δ<math><mtext>T</Mtext><mtext>′→</mtext><mtext>T</Mtext><msup><mi></Mi><mn>*</Mn></Msup><mtext>→</mtext><mtext>T</Mtext><mtext>, </Mtext><mtext>in Pr</Mtext><msub><mi></Mi><mn>2−x</Mn></msub><mtext>Sr</Mtext><msub><mi></Mi><mn>x</Mn></msub><mtext>CuO</Mtext><msub><mi></Mi><mn>4−δ</Mn></Msub></Math>, *Phys. C*, 1992, **192**(3), 362–371, DOI: **10.1016/0921-4534(92)90842-Z**.

60 N. V. Lyskov, M. S. Kaluzhskikh, L. S. Leonova, G. N. Mazo, S. Y. Istomin and E. V. Antipov, Electrochemical Characterization of Pr2CuO4 Cathode for IT-SOFC, *Int. J. Hydrogen Energy*, 2012, **37**(23), 18357–18364, DOI: **10.1016/j.ijhydene.2012.09.099**.

61 H. Li, Z. Cai, Q. Li, C. Sun and H. Zhao, Electrochemical Investigation of Pr2CuO4-Based Composite Cathode for Intermediate-Temperature Solid Oxide Fuel Cells, *J. Alloys Compd.*, 2016, **688**, 972–977, DOI: **10.1016/j.jallcom.2016.05.350**.

62 J. D. Sullivan, D. J. Buttrey, D. E. Cox and J. Hriljac, A Conventional and High-Resolution Synchrotron X-Ray Diffraction Study of Phase Separations in Pr2NiO4+δ, *J. Solid State Chem.*, 1991, **94**(2), 337–351, DOI: **10.1016/0022-4596(91)90200-2**.

63 A. P. Tarutin, N. A. Danilov, A. A. Kalinin, A. A. Murashkina and D. A. Medvedev, Ba-Doped Pr2NiO4+δ Electrodes for Proton-Conducting Electrochemical Cells. Part 1: Structure, Mechanical, and Chemical Properties, *Int. J. Hydrogen Energy*, 2023, **48**(59), 22531–22544, DOI: **10.1016/j.ijhydene.2022.11.175**.

64 S. M. Aspera, M. Sakaue, T. D. K. Wungu, M. Alaydrus, T. P. T. Linh, H. Kasai, M. Nakanishi and T. Ishihara, Analysis of Structural and Electronic Properties of Pr2NiO4 through First-Principles Calculations, *J. Phys.:Condens. Matter*, 2012, **24**(40), 405504, DOI: **10.1088/0953-8984/24/40/405504**.

65 T. H. AlAbdulaal, M. AlShadidi, M. S. A. Hussien, G. Vanga, A. Bouzidi, S. Rafique, H. Algarni, H. Y. Zahran, M. S. Abdel-wahab and I. S. Yahia, Enhancing the Electrical, Optical, and Structure Morphology Using Pr2O3-ZnO Nanocomposites: Towards Electronic Varistors and Environmental Photocatalytic Activity, *J. Photochem. Photobiol., A*, 2021, **418**, 113399, DOI: **10.1016/j.jphotochem.2021.113399**.

66 K. Terakura, Magnetism, Orbital Ordering and Lattice Distortion in Perovskite Transition-Metal Oxides, *Prog. Mater. Sci.*, 2007, **52**(2), 388–400, DOI: **10.1016/j.pmatsci.2006.10.007**.

67 L. Pecher and R. Tonner, Deriving Bonding Concepts for Molecules, Surfaces, and Solids with Energy Decomposition Analysis for Extended Systems, *WIREs Comput. Mol. Sci.*, 2019, **9**(4), e1401, DOI: **10.1002/wcms.1401**.

68 G. te Velde and E. J. Baerends, Precise Density-Functional Method for Periodic Structures, *Phys. Rev. B: Condens. Matter Mater. Phys.*, 1991, **44**(15), 7888–7903, DOI: **10.1103/PhysRevB.44.7888**.

69 R. S. Mulliken, Self-Consistent Field Atomic and Molecular Orbitals and Their Approximations as Linear Combinations of Slater-Type Orbitals, *Rev. Mod. Phys.*, 1960, **32**(2), 232–238, DOI: **10.1103/RevModPhys.32.232**.

70 X. Wang, J. Wang, P. Wang, L. Li, X. Zhang, D. Sun, Y. Li, Y. Tang, Y. Wang and G. Fu, Engineering 3d–2p–4f Gradient Orbital Coupling to Enhance Electrocatalytic Oxygen Reduction, *Adv. Mater.*, 2022, **34**(42), 2206540, DOI: **10.1002/adma.202206540**.

71 X. Wang, Y. Tang, J.-M. Lee and G. Fu, Recent Advances in Rare-Earth-Based Materials for Electrocatalysis, *Chem Catal.*, 2022, **2**(5), 967–1008, DOI: **10.1016/j.checat.2022.02.007**.

72 A. J. Medford, A. Vojvodic, J. S. Hummelshøj, J. Voss, F. Abild-Pedersen, F. Studt, T. Bligaard, A. Nilsson and J. K. Nørskov, From the Sabatier Principle to a Predictive Theory of Transition-Metal Heterogeneous Catalysis, *J. Catal.*, 2015, **328**, 36–42, DOI: **10.1016/j.jcat.2014.12.033**.

73 H. Li, Y. Pan, D. Zhang, Y. Han, Z. Wang, Y. Qin, S. Lin, X. Wu, H. Zhao, J. Lai, B. Huang and L. Wang, Surface Oxygen-Mediated Ultrathin PtRuM (Ni, Fe, and Co) Nanowires Boosting Methanol Oxidation Reaction, *J. Mater. Chem. A*, 2020, **8**(5), 2323–2330, DOI: **10.1039/C9TA11745H**.

74 Z. Qi, C. Xiao, C. Liu, T. W. Goh, L. Zhou, R. Maligal-Ganesh, Y. Pei, X. Li, L. A. Curtiss and W. Huang, Sub-4 Nm PtZn Intermetallic Nanoparticles for Enhanced Mass and Specific Activities in Catalytic Electrooxidation Reaction, *J. Am. Chem. Soc.*, 2017, **139**(13), 4762–4768, DOI: **10.1021/jacs.6b12780**.